Luminescence mechanisms of Ag^+ cubic centres in strontium fluoride crystals

1994 J. Phys.: Condens. Matter 6 8931

(http://iopscience.iop.org/0953-8984/6/42/023)

J. Phys.: Condens. Matter 6 (1994) 8931–8947. Printed in the UK

Luminescence mechanisms of Ag^+ cubic centres in strontium fluoride crystals

P Boutinaud, A Monnier and H Bill

Département de Chimie-Physique, Sciences II, 30 Quai E Ansermet, 1211 Geneve 4, Switzerland

Received 4 April 1994, in final form 6 June 1994

Abstract. The spectroscopic properties of Ag^+-doped strontium fluoride crystals were investigated at various temperatures, using absorption and fluorescence spectroscopies. The system exhibits a strong ultraviolet emission upon excitation into the two principal absorption bands. The azimuthal dependence of the degree of polarization of this luminescence is analysed, as well as its dynamics. The monovalent silver ions are shown to substitute for a host cation, with cubic symmetry. This is the first reported example of a cubic coordination for the Ag^+ ions in an insulator. This cubic field, together with the strong ionic character of the framework, confers rather original spectroscopic properties to this system. The luminescence mechanisms are interpreted on the basis of the measured decay times and with the aid of energy diagram calculations. Two closed thermalized spin–orbit levels, with symmetry A_{2g} and T_{2g} respectively, are involved in the luminescence processes. The pure spin triplet A_{2g} only emits at low temperatures ($T < 15$ K), whereas the T_{2g} level ($\sim 2\%$ spin singlet character) emits in turn upon warming the crystal. One-dimensional configuration coordinate diagrams are proposed to interpret the peculiar temperature dependence of the emission band maximum.

1. Introduction

For several years now, the need for new tunable solid-state laser systems for visible or near-ultraviolet output has led to a multiplication of the experimental and theoretical work on Cu^+-activated insulators, essentially in alkali halide crystals [1–8], glasses [9–12] and more recently fluorides [13]. At the same time, some publications appeared on the isoelectronic Ag^+ ion [14–18], but never in alkaline-earth fluorides.

Despite strong similarities between these two ions—both are closed shells and exhibit parity-forbidden $d^{10} \leftrightarrow d^9s$ phonon-assisted transitions—great discrepancies exist and the rather good knowledge of the spectroscopic behaviour of Cu^+ in insulators does not guarantee an equivalently accurate description of the Ag^+ properties.

For instance, monovalent copper is sometimes found off-centre at a given site, because of its tendency to form linear coordination, whereas Ag^+ tends to stay on site. Further, the strong difference between their respective spin–orbit coupling constants (more than twice as large for the Ag^+ free ion) usually gives rise to more complex spectra in the case of monovalent silver, because of the resultant large spin–orbit coupling between spin singlet and triplet states.

Fluorides are well known to be good laser host materials because of their large electronic band gap and their chemical stability.

We report here the spectroscopic properties of monovalent silver in the substitutional cubic site of strontium fluoride crystals. The luminescence mechanisms are interpreted

0953-8984/94/428931+17$19.50

on the basis of luminescence decays, energy diagram calculations and with the help of configuration coordinate diagrams.

2. Experimental methods

For optical applications, the growth of oxygen-free Ag^+-doped fluoride crystals remains a particularly delicate operation. Its whole methodology is given in detail in [19].

A large part of the silver fluoride introduced decomposes during growth and deposits on the furnace walls. In addition, the chemical analysis of the silver centres in the crystals is difficult because of the very low solubility of fluorides in most solvents. As a consequence, the Ag^+ concentration in the samples is not known.

The as-grown crystals usually exhibit a strong silver concentration gradient and also a strongly inhomogeneous distribution of different absorbing centres. Metallic silver droplets and colloidal particles often precipitate at the bottom of the crystals and usually a yellow coloration appears at the ends [19]. Nevertheless, the whole central part of the samples often remains colourless.

Plates of about 2 mm thick were extracted from this colourless part, either by natural cleavage along the {(111)} planes or by cutting planes parallel to {(110)} or {(100)}. The parallel surfaces were then carefully polished for the optical studies.

The absorption spectra were recorded between 190 and 800 nm on a Cary 2300 equipped with an Oxford bath cryostat for low-temperature measurements. Excitation and emission spectra were obtained by using a home-made computer-scannable spectrofluorimeter. The excitation light of a 300 W Varian xenon lamp was selected with an H20 monochromator (from Instrument SA) and focused on the sample. The 90° luminescence was dispersed using a double-prism Cary 1605 monochromator and detected with a Hamamatsu R928 photomultiplier tube (PMT) followed by an SR 530 lock-in amplifier.

An 8CC bath cryostat from Cryo-Industries was utilized for low-temperature analyses. The luminescence spectra were systematically corrected from the source, the monochromators and the PMT spectral responses.

The lifetime measurements were made as a function of temperature in a range between 2.2 and 300 K, using a 30 W Hamamatsu pulsed xenon lamp (10 Hz repetition rate) as a light source. The excitation light was selected with appropriate UV narrow-band filters.

The luminescence decays were recorded with the help of a Lecroy 9420 digital oscilloscope and transferred to a computer.

The azimuthal dependence of the polarized luminescence was performed at room temperature on the basis of Feofilov's work [20, 21]. The excitation light of a deuterium lamp was selected by a narrow-band filter (centred around 225 nm) and linearly polarized using a fused-silica Glan polarizer.

Sample plates were mounted on a home-made rotator in a way such that either the (111), the (110) or the (100) face of the crystal was oriented perpendicular to the UV light beam. This beam was focused onto the sample. The resulting circular spot was smaller than 2 mm in diameter.

The luminescence intensity is measured collinear ($I_\parallel$) or perpendicular ($I_\perp$) to the incident linear polarization (by using an HNPB Polaroid filter), as a function of the crystal rotation angle θ. The intensity ($I_\perp$) was corrected to compensate for the monochromator and PMT dichroism.

3. Experimental results

3.1. Absorption spectra

Absorption spectra of a large number of SrF_2:Ag^+ thin plates were recorded in order to check the reproducibility of the results. Figure 1 displays the absorption spectrum at $T = 10$ K of a 2.2 mm thick plate. It exhibits two intense bands labelled A and B including two shoulders in the interval 190–240 nm, and a long tail up to about 350 nm. The fit of this spectrum with a Simplex-type procedure [22] yielded 12 elementary Gaussian-shaped bands. Table 1 reports their spectral characteristics. The optical density of all the bands decreases strongly when the temperature is lowered, showing the vibronic character of the transitions involved (see insert of figure 1). The undoped samples show no significant absorption in the spectral range explored.

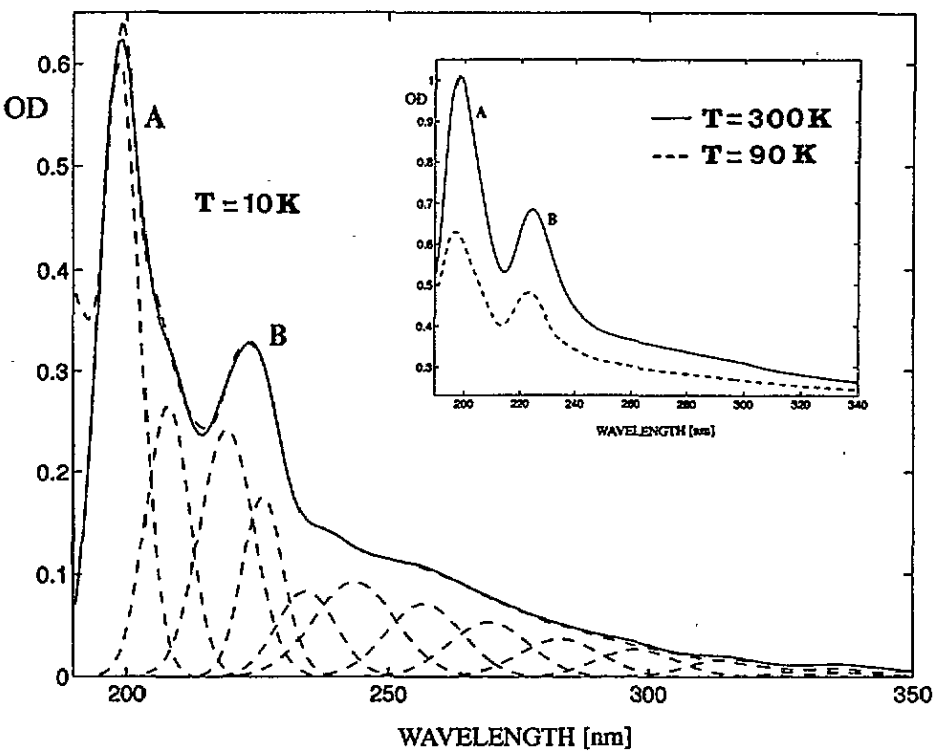

Figure 1. Absorption spectrum at $T = 10$ K for 2.2 mm SrF_2:Ag^+ plate and spectral decomposition into elementary Gaussian bands: experimental (----) and fitted spectrum (——). Inset: absorption spectrum of SrF_2:Ag^+ plate at $T = 300$ and 80 K.

3.2. Luminescence spectra

All the examples exhibit several luminescences with various relative intensities [23]. Among them, one is predominant and occurs in the UV range. It is observed under excitation in either the A or the B bands. Figure 2 displays the corresponding excitation and emission spectra at $T = 6$, 90 and 300 K. The excitation spectra were systematically decomposed into a sum of

Table 1. Optical density, half-width and position of the maximum of the elementary Gaussian absorption bands after fitting and spectral decomposition.

λ_{max} (nm)	Energy (cm^{-1})	FWHM (cm^{-1})	OD
198.5	50378	2620	0.60
207.7	48146	2445	0.26
219.0	45662	2420	0.24
226.0	44248	1970	0.17
234.3	42680	2440	0.08
243.5	41068	3110	0.09
256.8	38941	2370	0.07
269.1	37161	2325	0.05
282.8	35360	2360	0.03
297.6	33602	2150	0.027
314.8	31766	1750	0.02
334.6	29886	1695	0.009

Gaussian bands for the three temperatures, as described above. Their spectral characteristics are collected in tables 2 and 3. The agreement between fitted and experimental spectra is better than 99.5%.

At low temperature, the spectrum consists of five bands, which correspond in position (to the accuracy of the fits) to the first five entries of table 1. Their maximum position is nearly temperature-independent, but all of them broaden upon warming. The A bands (200 and 207 nm), however, widen much less than the others.

At the same time, the relative intensity of the bands changes slightly. According to the fit, the 221 nm band gradually decreases when the temperature is raised, and is totally unobservable in the 300 K spectrum. Simultaneously, the relative intensity of the A bands is enhanced. At any temperature, the intensity of the A bands with respect to that of the B bands is always higher in the absorption spectrum than in the excitation spectrum.

The UV luminescence, peaking at around 315 nm, is strongly asymmetric, even when plotted in an energy scale. This shape is intrinsic to the emission since the same excitation spectrum is generated whatever the side of the emission analysed.

At $T = 6$ K, the Stokes shift Δ is estimated at some 12 185 cm^{-1}. Here, Δ represents the energy difference between the barycentre of the lowest excitation bands and the maximum of the emission band. The value of the corresponding Huang–Rhys factor S is around 20. This factor gives the mean number of quanta of phonons emitted after the optical transition. It is approximately given at 0 K by

$$S \sim 2 \log 2 [\Delta/\sigma(0)]^2.$$

Note that this equation is available within the approximation of the same force constants (k_{exc} and k_{grd}) for both excited and ground states.

As the crystal is warmed up, the luminescence maximum first shifts to higher energies, then shifts back towards the low-energy side. This reproducible effect is observed upon excitation into either A or B bands. In contrast, the emission half-width (FWHM) $\sigma(T)$ increases regularly with temperature but cannot be described using

$$\sigma(T) = \sigma(0)[\coth(\hbar\omega/kT)]^{1/2}$$

(see insert of figure 2(*d*)).

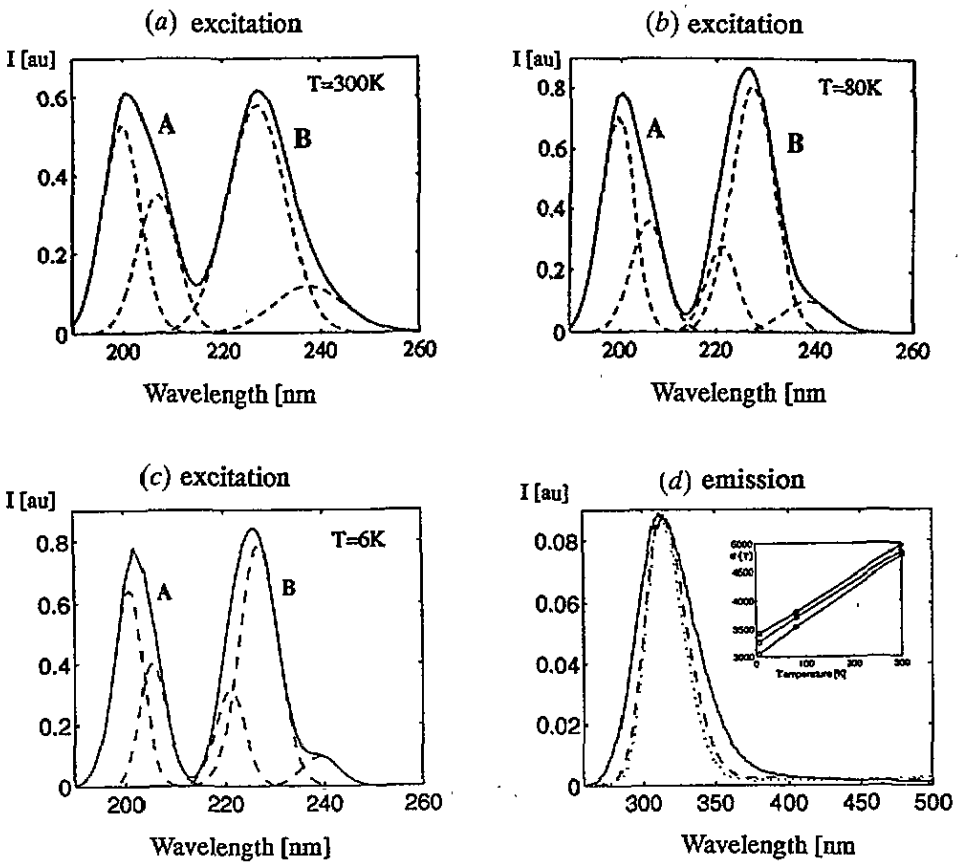

Figure 2. Excitation spectra at $T = 300$ (*a*), 80 (*b*) and 6 K (*c*) for $\lambda_{em} = 300$ nm. Spectral decomposition into elementary Gaussian bands (----). Fitted and experimental spectra are exactly superimposed (——). (*d*) Normalized emission spectra at $T = 300$ (——), 80 (----) and 6 K (·····) for $\lambda_{exc} = 200$ nm. Inset: temperature dependence of the luminescence bandwidth upon excitation at 200 nm (top), 215 nm (middle) and 230 nm (bottom).

Table 2. Half-width and position of the maximum of the elementary Gaussian excitation bands at $T = 300$, 80 and 6 K, after fitting and spectral decomposition, for $\lambda_{em} = 300$ nm.

$T = 300$ K			$T = 80$ K			$T = 6$ K		
λ_{max} (nm)	Energy (cm^{-1})	FWHM (cm^{-1})	λ_{max} (nm)	Energy (cm^{-1})	FWHM (cm^{-1})	λ_{max} (nm)	Energy (cm^{-1})	FWHM (cm^{-1})
199.6	50 100	2290	199.6	50 100	2040	200	50 000	2030
207	48 310	2220	206	48 540	2000	205.4	48 685	1690
—	—	—	221	45 250	1550	220.9	45 270	1610
227	44 050	2585	227	44 050	1940	226.8	44 090	1700
238	42 015	2990	239	41 840	2010	239.1	41 820	1540

3.3. Polarized luminescence

The azimuthal variation of the degree of polarization $P(\theta)$ of the UV luminescence, for three oriented plates, is defined as usual by

$$P(\theta) = [I_{\parallel}(\theta) - I_{\perp}(\theta)]/[I_{\parallel}(\theta) + I_{\perp}(\theta)].$$

Table 3. Half-width and position of the maximum of the emission band at 300, 80 and 6 K for $\lambda_{exc} = 200$ nm.

	$T = 300$ K	$T = 80$ K	$T = 6$ K
Energy (cm^{-1})	31 780	32 020	31 805
FWHM (cm^{-1})	4845	3710	3265

Whatever the incident face, $P(\theta)$ remained constant within experimental precision and was nearly equal to zero (meaning $I_{\parallel} \simeq I_{\perp}$). These results indicate that the UV centre possesses cubic symmetry, involving an inversion centre.

3.4. Luminescence decays

The temperature dependence of the UV luminescence lifetime is shown in figure 3. All the decays have purely exponential form. The evolution of the time constant τ can be parametrized as a function of T using the three-level model first described by Pedrini [8]:

$$\tau^{-1} = \frac{A_{31} + (g_2/g_3)A_{21}\exp(-\epsilon/kT)}{1 + (g_2/g_3)\exp(-\epsilon/kT)}. \tag{1}$$

In this expression, A_{31} and A_{21} represent the radiative transition probabilities of the two lowest excited levels ($1\Gamma_2$ and $1\Gamma_5$; see next section), separated by the quantum ϵ. A_{31} is relative to the lowest emitting level ($1\Gamma_2$) and is evaluated as the inverse of τ at 0 K. The emitting state degeneracies g_3 (= 1 for $1\Gamma_2$) and g_2 (= 3 for $1\Gamma_5$) must be introduced into Pedrini's original equation to respect the multiplicity of the sublevels. The full curve presents the best fit to the experimental data, from which the following parameters were extracted: $A_{31} = 7763\ s^{-1}$, $A_{21} = 112\,000\ s^{-1}$ and $\epsilon = 40\ cm^{-1}$.

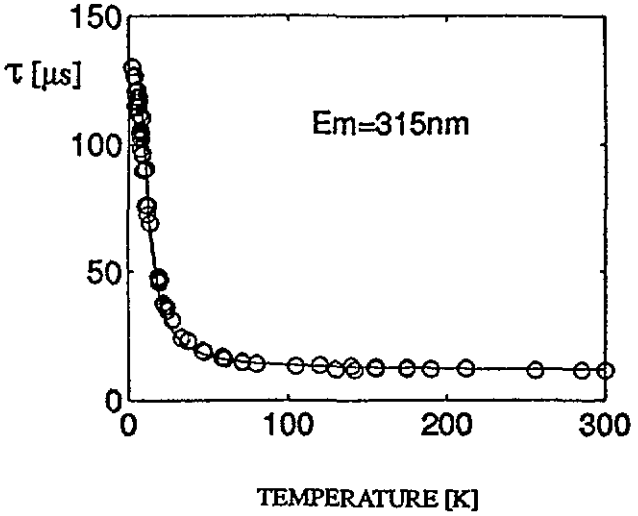

Figure 3. Temperature dependence of the UV luminescence lifetime (λ_{exc} around 225 nm and $\lambda_{em} = 315$ nm).

The oscillator strength of the luminescence transition $f = A_{31}mc^3/8\pi^2e^2\nu^2$ (where ν represents the energy of the emission maximum at low temperature) is then estimated at some 10^{-5}. The same dependence, with the same parameters, is obtained also for $\lambda_{em} = 300$ nm and $\lambda_{em} = 340$ nm. No thermal quenching of the luminescence is observed at or below room temperature.

3.5. Energy diagram calculation

A calculation has been performed on the single Ag^+ $4d^9 5s$ excited configuration using the following Hamiltonian:

$$H = H_{re} + V + \lambda(LS)$$

with

$$V = B^4\left[C_0^4 + \sqrt{(5/14)}(C_4^4 + C_{-4}^4)\right].$$

The antisymmetrized wavefunctions forming the basis set are Slater-type determinants $\psi = [\varphi_d, \varphi_s]$, where φ_s represents the 5s atomic orbital (AO) and φ_d represents either θ, ϵ, ξ, η or ζ real d orbitals, respectively defined by the standard spherical harmonics. We assume d orbitals ($\varphi_{d\upsilon}$ with $\upsilon = -2, -1, \ldots, +2$) with a common radial part:

$$\theta = \varphi_{4d0}/(Y_2^0)$$

$$\epsilon = \left(1/\sqrt{2}\right)(\varphi_{4d2} + \varphi_{4d-2})/\left[\left(1/\sqrt{2}\right)(Y_2^2 + Y_2^{-2})\right]$$

$$\xi = \left(i/\sqrt{2}\right)(\varphi_{4d1} + \varphi_{4d-1})/\left[\left(i/\sqrt{2}\right)(Y_2^1 - Y_2^{-1})\right]$$

$$\eta = \left(-1/\sqrt{2}\right)(\varphi_{4d1} - \varphi_{4d-1})/\left[\left(-1/\sqrt{2}\right)(Y_2^1 + Y_2^{-1})\right]$$

$$\zeta = \left(-i/\sqrt{2}\right)(\varphi_{4d2} - \varphi_{4d-2})/\left[\left(-i/\sqrt{2}\right)(Y_2^2 - Y_2^{-2})\right].$$

Among the 20 orthonormalized functions ψ^i of the basis (i stands for θ, ϵ, ξ, η or ζ), five are spin singlets ψ_S^i and 15 are spin triplets ψ_T^i. The singlet wavefunctions have the form

$$\psi_S^i = \left(1/\sqrt{2}\right)([\varphi_d^+, \varphi_s^-] - [\varphi_d^-, \varphi_s^+])$$

(where $+$ and $-$ stand for $M_s = +1$ and $M_s = -1$) whereas the triplet wavefunctions have the form

$$\psi_{T+}^i = [\varphi_d^+, \varphi_s^+]$$

$$\psi_{T-}^i = [\varphi_d^-, \varphi_s^-]$$

$$\psi_{T0}^i = \left(1/\sqrt{2}\right)([\varphi_d^+, \varphi_s^-] + [\varphi_d^-, \varphi_s^+]).$$

The choice of the basis gives diagonal crystal-field (V) and electronic-repulsion (H_{re}) Hamiltonians. The resulting matrix Π of dimension 20×20 decomposes into a 4×4 matrix, each made up by 5×5 submatrices M. The complete matrix is given in the appendix.

The diagonalization of the matrix (performed with the aid of a MATLAB program) gives multielectronic eigenfunctions Φ expressed as linear combinations of the ψ^i determinants. The corresponding eigenvalues are therefore the energies of the spectroscopic terms.

The Π matrix contains four unknown parameters: the spin–orbit constant λ, the crystal-field parameter D_q and the conventional Coulomb and exchange integrals J and K. However, as we do not compute the transition energies between the d^{10} and d^9s configurations, knowledge of the J integral is not needed, since its action is only to shift the energy barycentre of the whole excited configuration with respect to the ground-state one. For this reason, J will be neglected and the energy of the lowest term will be arbitrarily assigned to 0. Accordingly, only the energy differences between terms inside the d^9s configuration will be significant. In the following, the remaining parameters are considered as adjustable to the experimental data.

3.5.1. Evaluation of λ and K in the Ag^+ free ion. For the Ag^+ free ion ($D_q = 0$), the energy differences between $^3D_3$, $^3D_2$, $^3D_1$ and $^1D_2$ terms [24] give an experimental set of data that can be compared to the calculated eigenvalues. Then, a simple minimization Nelder-type procedure [22] is able to furnish the best set of λ and K. Very good agreement is obtained with $\lambda = 1819$ cm^{-1} and $K = 1931$ cm^{-1} (the mean value of the relative deviations between forecast and experimental data is around 1%).

3.5.2. Evaluation of λ, K and Dq parameters in the cubic SrF_2:Ag^+ crystals. The same procedure was used to calculate the values of λ, K and Dq of Ag^+ at the cubic sites of the crystal. Here, we get the experimental data from the energy differences between the first five successive absorption maxima extracted from table 1. After the minimization process, the following parameters are available:

$$\lambda = 1203 \text{ cm}^{-1} \qquad K = 1597 \text{ cm}^{-1} \qquad 10D_q = 3195 \text{ cm}^{-1}.$$

The spin–orbit constant is reduced by some 34% with respect to the free-ion value, but remains a very important perturbation, with about the same magnitude as K, the exchange integral. In contrast, the crystal-field parameter is quite low (only twice the value of K), but it is consistent with the ionic character of the network and the eightfold cubic coordination of the impurity in it.

Note that these results depend critically on the determination of the position of the bands, and thus on the quality of the decomposition of the experimental spectra into the Gaussians. We did not study the quality of the (though reproducible) minima obtained by our minimazation program because, intrinsically, our experiments do not allow for better spectral resolution.

Table 4. Comparison of the experimental and calculated energy differences between the absorbing cubic Ag^+-doped SrF_2 terms for $4d^95s^1$ excited configuration.

	Energy (cm^{-1})		
Terms	Expt.	Calc.	Difference (cm^{-1})
$2\Gamma_3$–$3\Gamma_5$	2208	2070	138
$3\Gamma_5$–$2\Gamma_5$	2507	2682	−175
$2\Gamma_5$–$1\Gamma_3$	1414	1743	−329
$1\Gamma_3$–$1\Gamma_5$	1567	1124	443
$2\Gamma_3$–$1\Gamma_5$	7697	7620	57

The results of the calculation performed using these specific parameters are reported in table 4, where they are compared to the experimental values. The symmetry-group labels of the spin–orbit terms were determined by examining the corresponding eigenfunctions Φ. Most of the terms Γ_i are linear combinations of $|^{1,3}E_g\rangle$ and $|^{1,3}T_{2g}\rangle$ states (table 5). For each component Γ_i, the percentage of spin singlet character is evaluated.

Table 5. Computed spectroscopic terms for $4d^9 5s^1$ configuration in the case of Ag^+ in O_h symmetry. Indication of their energy, their spin singlet character and of the symmetry of the wavefunctions involved.

Spin–orbit term	Wavefunctions involved							Singlet percentage	Energy (cm^{-1})
	$\|^1E_g\rangle$	...	$\|^1T_{2g}\rangle$	...	$\|^3E_g\rangle$	...	$\|^3T_{2g}\rangle$		
$2\Gamma_3$ (E_g)	0.97		0		0		0.23	94.5	7947
$3\Gamma_5$ (T_{2g})	0		0.69		0.69		0.22	47.5	5876
$2\Gamma_4$ (T_{1g})	0		0		0.91		0.41	0	5065
$2\Gamma_5$ (T_{2g})	0		0.71		0.71		0	50.0	3195
$1\Gamma_3$ (E_g)	0.23		0		0		0.97	5.4	1452
$1\Gamma_4$ (T_{1g})	0		0		0.41		0.91	0	1139
$1\Gamma_5$ (T_{2g})	0		0.15		0.27		0.97	2.2	327
$1\Gamma_2$ (A_{2g})	0		0		0		1	0	0

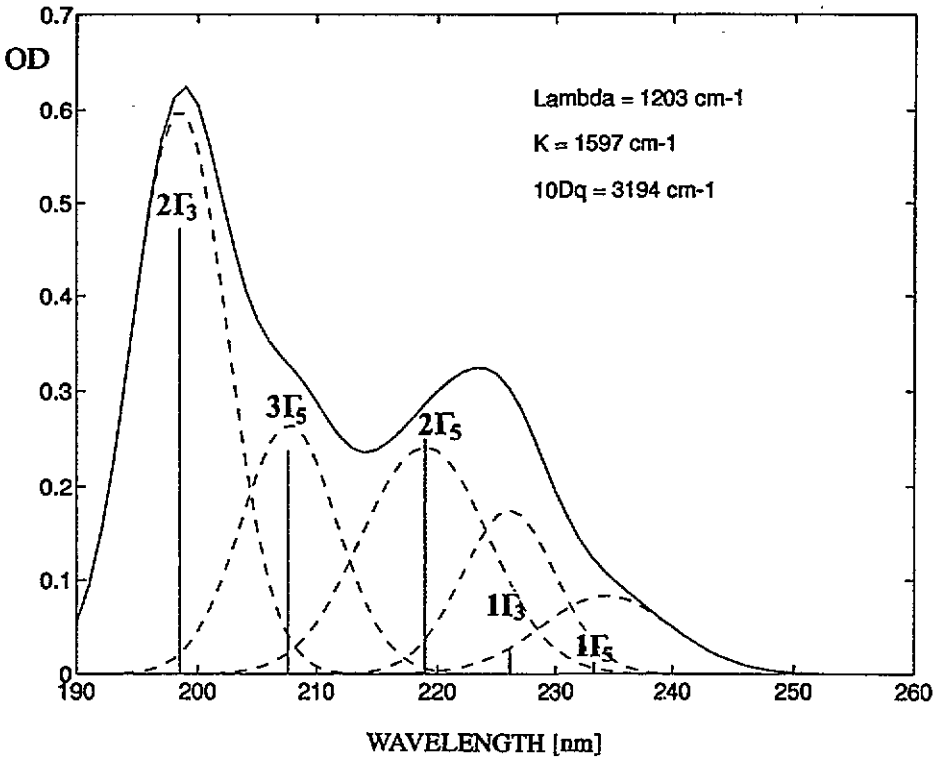

Figure 4. Comparison between the experimental absorption spectrum at 10 K, the first five transitions only (curves) and the calculated spectrum (sticks).

Figure 4 shows the comparison between the absorption spectrum (taking into account the first five transitions only) and the calculated one being represented by the sticks. Their length is proportional to the percentage of singlet character of the terms. The ground state is expected to be the pure spin singlet term $1\Gamma_1$. This enables five spin-allowed singlet–singlet transitions. In order to facilitate the comparison, the whole theoretical $4d^9 5s$ configuration has been raised by 42 467 cm^{-1}.

4. Discussion

No luminescence was detected in the pure SrF_2 crystal, even at low temperature. Accordingly, the origin of luminescence in SrF_2:Ag^+ must be due only to the presence of silver. Several arguments give credence to the attribution of the UV centre to an Ag^+ ion in a pure cubic environment:

(i) When embedded in NaCl [14], KCl [14] or NaF [25], the Ag^+ centre gives rise to a series of characteristic absorption bands in the UV range, very similar to our A and B bands. In these alkali halide hosts, Ag^+ always substitutes for the cation, without any need of charge compensation, and thus possesses pure O_h symmetry.

(ii) The necessity to use a three-level model to parametrize the temperature dependence of the UV luminescence lifetime is a general feature for single Ag^+ or Cu^+ ions in insulators [1, 8, 17].

(iii) After x-ray irradiation of the Ag^+-doped samples, a strong electron spin resonance (ESR) signal, typical of Ag^{2+} ions in Jahn–Teller (JT) distorted cubic symmetry, is observed [26] with a concomitant decrease of the intensity of the A and B bands [19].

(iv) The results of the polarized luminescence measurements give additional support since they provide an experimental proof of the global isotropy of the Ag^+ surrounding. Therefore, in this fluoride network, the symmetry of the reported monovalent silver centre is cubic.

(v) Finally, the results of the calculations give satisfactory confirmation of our hypothesis. Five transitions were expected from the experimental data and from [15] and five partly spin-allowed transitions are obtained by computation. The respective intensity ratios agree rather well.

Of course, this agreement is not excellent, especially if we deal with the low-energy side of the spectrum (226 and 234 nm bands). Several reasons account for that:

(i) In this latter spectral range a non-negligible overlap exists between the Ag^+ bands and bands belonging to other centres [23], which renders difficult an accurate estimate of the real intensity of the Ag^+ bands.

(ii) The interaction with the $4d^9 5p$ configuration has not been taken into account. Despite a rather weak crystal field ($\sim$ 3195 cm^{-1}), which tends to minimize this effect, this interaction with the 5p orbitals induces some symmetry-allowed intensity contributions.

(iii) Further, the vibronic coupling with low-frequency vibrations of odd symmetry has been neglected, though they contribute in a non-negligible way to the experimental intensity ratios.

Two different locations of the cubic Ag^+ centre are possible in the fluoride network. Both involve a non-local charge compensation. Either Ag^+ substitutes Sr^{2+} and forms the electron-donor centre $(Ag^+_{Sr^{2+}})^\circ$ or Ag^+ occupies an interstitial site thereby becoming the electron-acceptor species $(Ag^+_{\square})'$.

The rather small value of the S factor in this ionic network suggests a small Δr shift of the excited configuration curve with respect to the ground-state one. This assumption is consistent with the absence of thermal quenching of the luminescence up to at least room temperature (see figure 3).

Consequently, the $(Ag^+_{Sr^{2+}})^\circ$ centre is a much more favourable option than the $(Ag^+_{\square})'$ structure. Dealing with simple steric arguments, we add the following remark. The substitution of Sr^{2+} (ionic radius 1.25 Å) by Ag^+ (ionic radius 1.30 Å) leads to a much reduced Δr shift, because the lattice has the tendency to compress the impurity. The opposite situation involves a more spacious interstitial site, which would need an important Δr shift to accommodate the Ag^+ ion.

4.1. Luminescence mechanisms

A general feature of monovalent copper and silver introduced into alkali halides is that the luminescence dynamics involves the three-level model (see section 3.4). The Ag^+ ion embedded in the fluoride network presents this property too.

After absorption into the Γ_3 and Γ_5 excited states of the $4d^95s^1$ configuration, the relaxation processes release the system into the two lowest excited states $1\Gamma_2$ and $1\Gamma_5$, in mutual thermal equilibrium. From equation (1), the contribution of each of the levels to the transition probability can be expressed as

$$P_{31} = \frac{A_{31}}{1 + 3\exp(-\epsilon/kT)} \qquad \text{for } 1\Gamma_2$$

and

$$P_{21} = \frac{3A_{21}\exp(-\epsilon/kT)}{1 + 3\exp(-\epsilon/kT)} \qquad \text{for } 1\Gamma_5.$$

P_{31} and P_{21} are equal for $T = 15$ K. Below this temperature, P_{31} is preponderant ($P_{31}/P_{21} \simeq 340$ at 6 K) and only the pure spin triplet $1\Gamma_2$ (A_{2g}) emits.

Above this temperature, the next higher $1\Gamma_5$ (T_{2g}) level starts to be populated. Then, this level emits with an oscillator strength higher than the one of $1\Gamma_2$, because of its 2.2% spin singlet character. This assumption is experimentally confirmed by the ratio $A_{21}/A_{31} \gg 1$. At 80 K, $P_{21} \simeq 21P_{31}$ and $1\Gamma_5$ becomes the principal emitting state.

Upon warming, the maximum position of the luminescence band is shifted towards high energies, by some 215 cm^{-1}, and then is shifted back to the low-energy side (table 3). Such a behaviour is not frequent. Indeed, in the case of a single emitting level (here $1\Gamma_5$), one should expect a regular monotonic shift of the emission maximum.

From this result, and additionally the luminescence dynamics and the energy diagram calculations, the respective curvature of the excited $1\Gamma_2$ and $1\Gamma_5$ configuration curves can be qualitatively deduced. For this, the role of the (probably weak but not totally negligible) covalency of the Ag–F bond has to be considered.

In the cubic symmetry, the silver $1\Gamma_5$ (T_{2g}) wavefunctions are partly implied in the (σ and π) weak bonding with the hybridized s^2p^6 functions of the ligands, via a probable $s^2p^3d^3$ hybridization. In contrast, the $1\Gamma_2$ (A_{2g}) wavefunction is less involved in this hybridization and thus probably participates even less to the metal–ligand interaction. As a consequence, the slight curvature of the $1\Gamma_5$ excited potential curve (given by $U_{exc} = 1/2k_{exc}\Delta r^2$ in the harmonic approximation) should be more pronounced than that of $1\Gamma_2$ (in other words, $k_{exc}(1\Gamma_5) > k_{exc}(1\Gamma_2)$).

Therefore, during the $d^{10} \rightarrow d^9s$ transition, the promotion of an electron, from t_{2g}-like bonding orbitals to the next upper antibonding molecular orbital (MO), involves a perturbation of the ground-state electronic distribution, thus leading to a slight increase of the metal–fluoride distance in the excited state ($\Delta r > 0$). Within this model, the magnitude of this ligand repulsion effect is expected to be weaker if the electron originates from the a_{2g} orbital.

A schematic illustration of the relative positions of these two excited states, with respect to the ground state, is reported in the configuration coordinate diagrams of figure 5, taking into account only the totally symmetric vibrational mode a_{1g} of the fluorides. Figure 5(*a*) includes an enlarged view of the two excited levels.

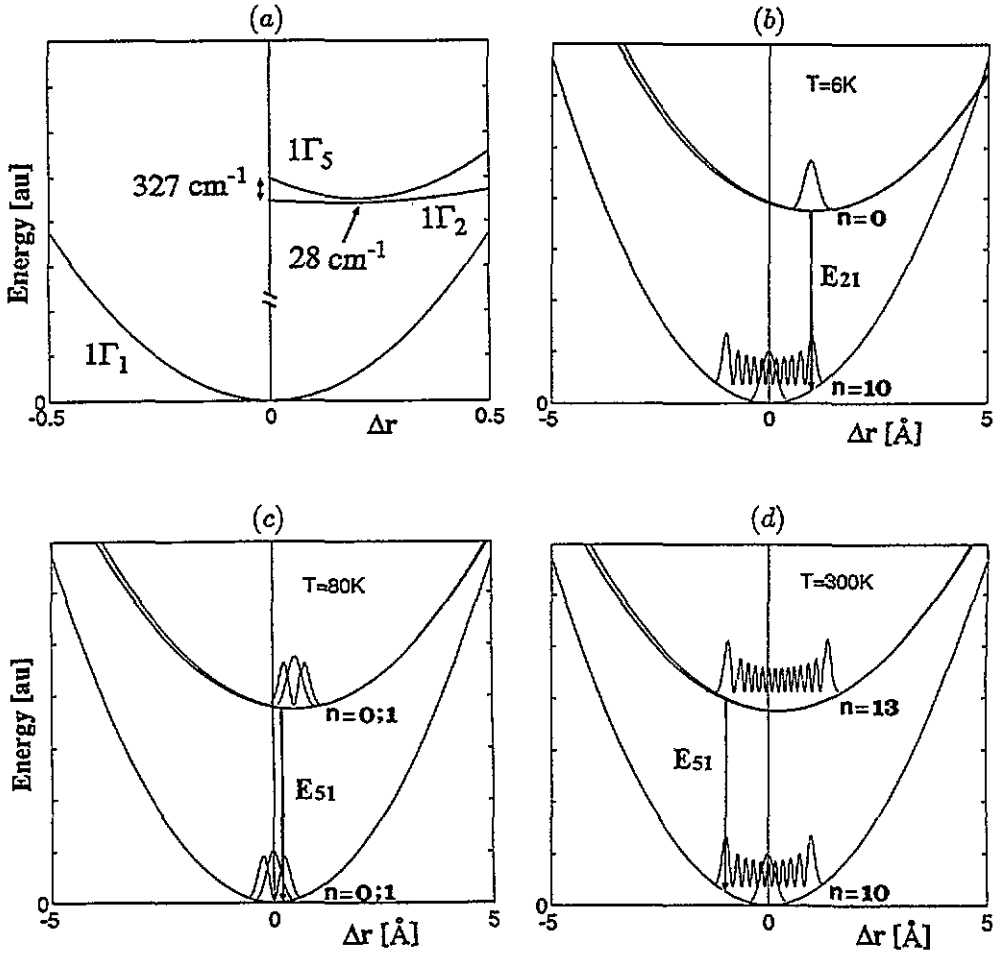

Figure 5. One-dimensional configuration diagrams illustrating the luminescence mechanisms form the two lowest excited levels $1\Gamma_5$ and $1\Gamma_2$. (*a*) Zoom showing the relative position of the two levels. In this picture, the energy scale is not respected. (*b*) Vibronic $1\Gamma_2(n = 0) \rightarrow 1\Gamma_1(n = 10)$ transition with energy E_{21} at $T = 6$ K. (*c*) Vibronic $1\Gamma_5(n = 0; 1) \rightarrow 1\Gamma_1(n = 0; 1)$ transition with energy $E_{51} > E_{21}$ at $T = 80$ K. (*d*) Vibronic $1\Gamma_5(n = 13) \rightarrow 1\Gamma_1(n = 10)$ transition with energy $E_{51}(300\ \text{K}) > E_{51}(80\ \text{K})$ at $T = 300$ K.

These diagrams (figures 5(*b*) to 5(*d*)) exhibit examples of vibrational density probabilities $|\chi_n(r)|^2$ of various vibrational levels n, for both $1\Gamma_5$ and $1\Gamma_1$ states. In the

harmonic approximation, the $\chi_n(r)$ wavefunctions are defined by

$$\chi_n(r) = N_n \exp[-\tfrac{1}{2}(r/a)]H_n(r/a).$$

Here N_n is a normalization constant, $H_n(r/a)$ is the Hermite polynomial, a represents the classical vibrational amplitude, given by $a = (h/M\omega)^{1/2}$, M is the mass of the eight vibrating fluorides and $h\omega$ is the vibrational quantum associated with these ions.

In the Franck–Condon approximation, the probability of a given optical transition is given by

$$P = \int \bar{\Phi}_{el}^{exc} \hat{\mu} \Phi_{el}^{grd} \, dr_{el} \int \bar{\chi}_n^{exc} \chi_n^{grd} \, dr_{nuc}$$

where $\hat{\mu}$ is the electric dipole operator and Φ_{el} are the electronic wavefunctions. The magnitude of this probability is then proportional to the overlap integral of the vibronic wavefunctions.

Note also that the values of the k_{exc} are expected to be quite small, in part because of the weak covalency in the bonding. Therefore, the curvatures of the potentials are small and the vibrational quantum $\hbar\omega_e$ is small, probably less than 150 cm^{-1}.

Within these diagrams, an interpretation of the thermal evolution of the luminescence maximum can be proposed.

At 6 K, the $1\Gamma_2 \rightarrow 1\Gamma_1$ transition occurs with an energy $E_{21}(6\ K)$. The $1\Gamma_5 \rightarrow 1\Gamma_1$ transition is highly improbable at this temperature (figure 5(*b*)).

When the temperature increases, two mechanisms are involved: the vibrational levels of $1\Gamma_5$ become thermally populated; the fluoride lattice undergoes a thermal expansion. It involves a global enhancement of the ground-state Ag–F equilibrium distance r_0, reducing further the Δr $(= r - r_0)$ shift in the excited state.

At 80 K, only the first two vibrational levels ($n = 0$ and $n = 1$) are efficiently populated. The overlap between the vibrational densities of the excited and the ground state, respectively, occurs at a Δr shift closer to 0. The energy of the $1\Gamma_5 \rightarrow 1\Gamma_1$ transition increases ($E_{51}(80\ K) > E_{21}(6\ K)$) and the emission maximum shifts towards the high-energy side (figure 5(*c*)).

At room temperature, the Δr shift still reduces (but remains positive) and higher vibrational levels ($n > 2$) are more strongly populated. Therefore, the $1\Gamma_5 \rightarrow 1\Gamma_1$ transition arises from a high $\chi_n(r)$ state. In this situation, the overlap with the ground-state vibrational density is maximum at $\Delta r < 0$ (figure 5(*d*)). The energy of the transition then decreases ($E_{51}(300\ K) < E_{51}(80\ K)$). As a result, the emission broadens and its maximum is shifted to the low-energy side.

Note that the point group of the $(AgF_8)^{7-}$ cluster in its excited state is not known and may not remain purely cubic, since a trigonal $T_{2g} \otimes t_{2g}$ JT effect occurs in the limiting case of Ag^{2+} ions in SrF_2 [26]. This effect may induce great discrepancies between $1\Gamma_2$ and $1\Gamma_5$ sublevels, which could strongly perturb the luminescence mechanisms.

Nevertheless, as there was no experimental evidence of this effect in our Ag^+ absorption and excitation spectra, the use of a one-dimensional diagram seemed justified in this first approach.

In the 6 K excitation spectra, the respective magnitude of the A and B bands is nearly the same, whereas, in the absorption spectrum, the intensity of A is about twice that of B. This suggests that absorption into the A bands is less efficient for the luminescence yield than into the B ones. Moreover, inside the excitation spectra, the contribution of the Γ_3

Table 6. Mean number p of highest energetic phonons needed to fill the various energy gaps between the successive Γ_i terms.

Gap	$2\Gamma_3$–$3\Gamma_5$	$3\Gamma_5$–$2\Gamma_4$	$2\Gamma_4$–$2\Gamma_5$	$2\Gamma_5$–$1\Gamma_3$	$1\Gamma_3$–$1\Gamma_4$	$1\Gamma_4$–$1\Gamma_5$	$1\Gamma_5$–$1\Gamma_2$
p	~ 5	~ 2	~ 5	~ 4	~ 1	~ 2	$\ll 1$

levels is always preponderant with respect to the Γ_5 one, despite the strong spin singlet character of this latter one.

One point is that luminescence is essentially a surface effect. Part of the energy of the radiation that penetrates too deeply into the bulk (leading to highest optical densities) is dispersed through phonons and, as a consequence, does not contribute to luminescence.

The other point is the important incidence of the multiphonon relaxation probabilities $A_{mp}(p)$ onto the luminescence quantum yield. This probability is expressed as:

$$A_{mp}(p) = A_0 \exp(-\gamma \Delta E) \left(\frac{\exp(\hbar\omega/kT)}{\exp(\hbar\omega/kT) - 1} \right)^p . \tag{2}$$

γ is a constant depending on the nature of the host, likewise A_0 is a constant containing the electron–phonon coupling, $\hbar\omega$ represents quanta with the highest phonon energy in the host (around 400 cm^{-1} for the LO modes in SrF_2), p stands for the number of phonons involved in the relaxation process and ΔE is the energy separating two successive levels between which the relaxation is operating.

Table 6 reports the approximate number of phonons p needed to fill the energy gap between pairs of successive levels of the $4d^9 5s^1$ configuration.

It is clear from equation (2) that, for a given phonon energy $\hbar\omega$, an increase of ΔE means an enhanced number of phonons (p) involved (since $\Delta E \simeq p\hbar\omega$). This leads to a diminution of $A_{mp}(p)$ and thus to a decrease of the luminescence yield.

For this reason, a smaller emission yield is expected from absorption into the A bands ($2\Gamma_3$ and $3\Gamma_5$) than into the B bands. This effect must also be present within the B bands: absorption into $2\Gamma_5$ should be less efficient ($p = 4$ between $2\Gamma_5$ and $1\Gamma_3$) than absorption into either $1\Gamma_3$ or $1\Gamma_5$. This is effectively confirmed by the excitation spectra.

However, an additional argument is necessary to understand why $2\Gamma_5$, which possesses 50% spin singlet, is so weak in the excitation spectra and gradually disappears as temperature grows, and why $1\Gamma_3$ (5.4%) is so dominant.

Here, the respective shapes of the $2\Gamma_5$ and $1\Gamma_3$ configuration curves, as well as the anharmonicity of the ground-state potential, are determining factors. The Γ_3 (E_g) wavefunctions participate to the π bonding with the fluorides somewhat more strongly than the Γ_5 ones, thus leading to more curved excited levels ($k_{exc}(1\Gamma_3) > k_{exc}(2\Gamma_5)$). A schematic illustration is reported in figure 6.

At rather low temperatures, competition exists between the multiphonon relaxation and a possible thermally assisted transfer between $2\Gamma_5$ and $1\Gamma_3$, which would lead to the population of $1\Gamma_3$ at the expense of $2\Gamma_5$ (processes (1) and (2)). When temperature increases, the transfer probabilities become preponderant and could even induce direct relaxation into the ground state $1\Gamma_1$ (process (3)), causing the quenching of the $2\Gamma_5$ excitation band.

5. Conclusion

When embedded into the SrF_2 network, the main proportion of monovalent silver stabilizes in a substitutional site with a pure cubic surrounding. This is one of the first reported examples of such a symmetry for this ion.

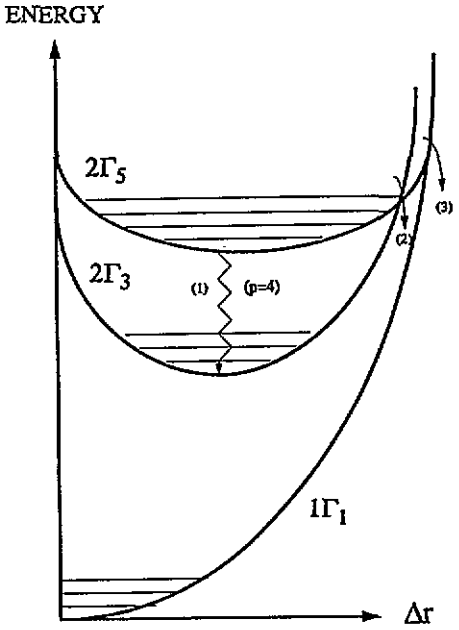

Figure 6. Schematic illustration of the possible transfer mechanisms between $2\Gamma_5$, $1\Gamma_3$ and $1\Gamma_1$: multiphonon relaxation (process (1)) and thermally assisted transfers (processes (2) and (3)).

The luminescence mechanisms of this cubic Ag^+ centre are interpreted on the basis of fluorescence dynamics and of energy diagram calculations.

The theoretical investigations provide a set of adjustable K, λ and D_q parameters, which can be utilized as starting parameters for further calculations involving lower symmetries.

Acknowledgments

Part of the contribution of one of the authors (HB) was worked out (and applied to Ag^+:NaF) during a stay at Princeton University, Chemistry Department, in autumn 1991. HB would like to thank warmly Professor D McClure for the hospitality he offered to accept him in his group, and extend his thanks to Princeton University. D Frauchiger contributed by growing single crystals, F Rouge realized mechanical construction work and J B Pluss and A Lonchamp contributed by realizing electronic devices needed. The aid of D Lovy on computer work was also much appreciated.

Appendix

$$\Pi \equiv \begin{array}{c} \begin{matrix} \psi_S & \psi_{T+} & \psi_{T0} & \psi_{T-} \end{matrix} \\ \begin{bmatrix} M_1 & M_2 & M_3 & M_4 \\ M_5 & M_6 & M_4 & M_0 \\ M_7 & M_8 & M_9 & M_4 \\ M_8 & M_0 & M_8 & M_{10} \end{bmatrix} \end{array}$$

with

$$M_1 = \begin{array}{c} \begin{matrix} \psi^\xi & \psi^\eta & \psi^\zeta & \psi^\theta & \psi^\epsilon \end{matrix} \\ \begin{bmatrix} J+K-4Dq & & & & \\ & J+K-4Dq & & & \\ & & J+K-4Dq & & \\ & & & J+K+6Dq & \\ & & & & J+K+6Dq \end{bmatrix} \end{array}$$

$$M_2 = \begin{bmatrix} & & -\lambda/\sqrt{8} & i\lambda\sqrt{3}/\sqrt{8} & i\lambda/\sqrt{8} \\ & & -i\lambda/\sqrt{8} & \lambda\sqrt{3}/\sqrt{8} & -\lambda/\sqrt{8} \\ \lambda/\sqrt{8} & i\lambda/\sqrt{8} & & & \\ -i\lambda\sqrt{3}/\sqrt{8} & -\lambda\sqrt{3}/\sqrt{8} & & & \\ -i\lambda/\sqrt{8} & \lambda/\sqrt{8} & & & \end{bmatrix}$$

$$M_3 = \begin{bmatrix} \cdot & i\lambda/2 & \cdot & \cdot & \cdot \\ -i\lambda/2 & \cdot & \cdot & \cdot & \cdot \\ \cdot & \cdot & \cdot & \cdot & i\lambda \\ \cdot & \cdot & \cdot & \cdot & \cdot \\ \cdot & \cdot & -i\lambda & \cdot & \cdot \end{bmatrix}$$

$$M_4 = \begin{bmatrix} & & -\lambda/\sqrt{8} & -i\lambda\sqrt{3}/\sqrt{8} & -i\lambda/\sqrt{8} \\ & & i\lambda/\sqrt{8} & \lambda\sqrt{3}/\sqrt{8} & -i\lambda/\sqrt{8} \\ \lambda/\sqrt{8} & -i\lambda/\sqrt{8} & & & \\ i\lambda\sqrt{3}/\sqrt{8} & -\lambda\sqrt{3}/\sqrt{8} & & & \\ i\lambda/\sqrt{8} & \lambda/\sqrt{8} & & & \end{bmatrix}$$

and

$$M_9 = \begin{bmatrix} J-K-4Dq & & & & \\ & J-K-4Dq & & & \\ & & J-K-4Dq & & \\ & & & J-K+6Dq & \\ & & & & J-K+6Dq \end{bmatrix}.$$

Concerning the other submatrices, we have $M_5 = M_2^T$, $M_7 = M_3^T$, $M_8 = M_4^T$, $M_6 = M_9 + M_3$ and $M_{10} = M_9 - M_3$. All the elements of the M_0 matrix are equal to 0. The well known crystal-field parameter Dq is equal to $B^4/21$ in the cubic field.

References

[1] Pedrini C and Jacquier B 1980 *J. Phys. C: Solid State Phys.* **13** 4791
[2] Payne S A, Goldberg A B and McClure D S 1983 *J. Chem. Phys.* **78** 3668
[3] Chermette H and Pedrini C 1982 *J. Chem. Phys.* **77** 2460
[4] Payne S A, Austin R H and McClure D S 1984 *Phys. Rev.* B **29** 32
[5] Berg J M and McClure D S 1989 *J. Chem. Phys.* **90** 3915
[6] Erwin S C and Lin C C 1989 *Phys. Rev.* B **40** 1892
[7] Moine B and Pedrini C 1984 *Phys. Rev.* B **30** 992
[8] Pedrini C 1978 *Phys. Status Solidi* **87** 273
[9] Zhang J C, Moine B, Pedrini C, Parent C and Le Flem G 1990 *J. Phys. Chem. Solids* **51** 933
[10] Boutinaud P, Duloisy E, Pedrini C, Moine B, Parent C and Le Flem G 1991 *J. Solid State Commun.* **94** 5100
[11] Liu H and Fuxi G 1986 *J. Non-Cryst. Solids* **80** 447

[12] Debnath R and Das S K 1982 *Chem. Phys. Lett.* **87** 508
[13] Pedrini C, Moine B and Bill H 1992 *J. Phys.: Condens. Matter* **4** 1615
[14] Fussgaenger K, Martiensen W and Bilz H 1965 *Phys. Status Solidi* **12** 383
[15] Moine B and Pedrini C 1984 *J. Physique* **45** 1491
[16] Atoussi B, Pedrini C, Moine B and Madej C 1985 *Phys. Status Solidi* **128** 683
[17] Pedrini C 1981 *Solid State Commun.* **38** 1237
[18] Pedrini C, Chermette H, Goldberg A B, McClure D S and Moine B 1983 *Phys. Status Solidi* B **120** 753
[19] Monnier A, Boutinaud P and Bill H *J. Phys. Chem. Solids* **55** 559
[20] Feofilov P P 1956 *J. Phys. Radium* **17** 656
[21] Feofilov P P 1954 *J. Exp. Theor. Phys. USSR* **26** 609
[22] Nelder J A and Mead R 1965 *Comput. J.* **7** 308
[23] Boutinaud P and Bill H to be published
[24] Moore C E 1949 *Atomic Energy Levels (US Nat. Bur. Stand. Circ. No 467)* (Washington, DC: US Govt. Printing Office)
[25] Bill H and McClure D S to be published
[26] Bill H, Lovy D and Hageman H 1989 *Solid State Commun.* **70** 511